

A High-Order Scheme for Image Segmentation via a modified Level-Set method

Maurizio Falcone*

Giulio Paolucci†

Silvia Tozza‡

May 28, 2022

Abstract

In this paper we propose an accurate method for image segmentation following the level-set approach. The method is based on an adaptive “filtered” scheme recently introduced by the authors. The main feature of the scheme is the possibility to stabilize an a priori unstable high-order scheme via a filter function which allows to combine a high-order scheme in the regularity regions and a monotone scheme elsewhere, in presence of singularities. The filtered scheme considered in this paper uses the local Lax-Friedrichs scheme as monotone scheme and the Lax-Wendroff scheme as high-order scheme but other couplings are possible. Moreover, we introduce also a modified velocity function for the level-set model used in segmentation, this velocity allows to obtain more accurate results with respect to other velocities proposed in the literature. Some numerical tests on synthetic and real images confirm the accuracy of the proposed method and the advantages given by the new velocity.

Keywords: Partial differential equations, Filtered scheme, segmentation problem, smoothness indicators.

1 Introduction

The Level-Set (LS) Method has been introduced by Osher and Sethian in the 1980s [24, 21] and then used to deal with several applications, e.g. fronts propagation, computer vision, computational fluids dynamics (see the monographs by Sethian [25] and by Osher and Fedkiw [20] for several interesting examples). This method is nowadays very popular for its simplicity and its capability to deal with topological changes. In fact, the main advantage of the level-set method is the possibility to easily describe time-varying objects, follow shapes that change topology, for example, when a shape splits in two, develops holes, or the reverse of these operations. In fact, a shape that changes its topology arriving to split into two objects is difficult to describe numerically in order to follow its evolution. It is much easier to consider the evolution in time of the shape through its level-set function. In \mathbb{R}^2 , the level-set method corresponds to representing

*Dipartimento di Matematica, “Sapienza” Università di Roma, P.le Aldo Moro, 5 - 00185 Rome, Italy (e-mail: falcone@mat.uniroma1.it)

†Dipartimento di Matematica, “Sapienza” Università di Roma, P.le Aldo Moro, 5 - 00185 Rome, Italy (e-mail: paolucci@mat.uniroma1.it)

‡Istituto Nazionale di Alta Matematica, U.O. Dipartimento di Matematica, “Sapienza” Università di Roma, P.le Aldo Moro, 5 - 00185 Rome, Italy (e-mail: tozza@mat.uniroma1.it)

The three authors are members of the INdAM Research group GNCS.

a closed curve Γ (such as the shape boundary in our case) using an auxiliary function φ , called the level-set function. Γ is represented as the zero-level set of φ by $\Gamma = \{(x, y) \mid \varphi(x, y) = 0\}$, and the level-set method manipulates Γ implicitly, through the function φ . This function φ will take positive values inside the region delimited by the curve Γ and negative values outside.

Here, we are interesting in following the evolution of a front that moves in its normal direction with a velocity $c(x, y)$. Since the velocity function depends only on the point (x, y) , this problem can be written in terms of a first order evolutive Hamilton-Jacobi equation of eikonal type

$$\begin{cases} v_t + c(x, y)|\nabla v| = 0, & (t, x, y) \in (0, T) \times \mathbb{R}^2, \\ v(0, x, y) = v_0(x, y), & (x, y) \in \mathbb{R}^2, \end{cases} \quad (1)$$

where v_0 must be a *proper representation* of the initial front Γ_0 , i.e. if we identify the first configuration of the front as the 0-level set of the viscosity solution, then we require

$$\begin{cases} v_0(x, y) < 0, & (x, y) \in \Omega_0, \\ v_0(x, y) = 0, & (x, y) \in \Gamma_0, \\ v_0(x, y) > 0, & (x, y) \in \mathbb{R}^2 \setminus \overline{\Omega_0}, \end{cases} \quad (2)$$

where Ω_0 is the region delimited by Γ_0 .

The front Γ_t at time $t > 0$ is defined as the 0-level set of the solution v of (1), i.e.

$$\Gamma_t := \{(x, y) : v(t, x, y) = 0\}. \quad (3)$$

The velocity $c(x, y)$ cannot change sign during the evolution, the orientation depends on the type of evolution (outward for an expansion and inward for a shrinking). In general, the level-set method can handle velocities depending on physical quantities in order to describe several phenomena, e.g.

- $c(t, x, y)$, isotropic growth with time varying velocity
- $c(t, x, y, \eta)$, anisotropic growth, dependent on normal direction
- $c(t, x, y, k)$, Mean Curvature Motion, with $k(t, x, y)$ mean curvature to the front at time t ,
- $c(t, x, y, v)$, velocity dependent on the level set.

Depending on the choice of the velocity, the front evolution will be described by first or second order PDEs. Here we will consider only first order problems (1) and velocities which depending only on the position.

In order to set our contribution into perspective, let us mention that the segmentation problem has been solved by various techniques which mainly rely on two different approaches: variational methods and active contour methods. For the first approach the interested reader can look at [7, 6] and the references therein. For the link between the two class of method, see [9]. As already said, we will apply the level set method based on (1) looking for an accurate numerical method. High-order methods have been proposed for (1) and most of them were based on non oscillatory local interpolation techniques that allow to avoid spurious oscillation around discontinuities of the solution and/or jumps in the gradient. These techniques were originally developed for conservation laws (see the seminal paper [13] and the references therein), the research activity on essentially non oscillatory (so called ENO) methods has been rather effective and a number of improvements have been proposed in e.g. [17, 15, 3] so that now ENO/WENO techniques are rather popular in many applications (see [27] for a recent survey). We should also mention that later these techniques were successfully applied to the numerical solution of Hamilton-Jacobi equations [22] opening the way to other applications. The reader interested in image processing will find in [1, 2] an application to image compression and in [26] an application to image segmentation. However, a general convergence theorem for ENO/WENO schemes is still missing and their application is a rather delicate issue. These limitations have motivated further investigations and a new class of high-order methods for evolutive Hamilton-Jacobi equations

have been proposed looking for a different approach based on “*filtered schemes*” introduced in this framework by Lions and Souganidis [16]. The class of filtered schemes is based on a simple coupling of a monotone scheme with a high-order accurate scheme. Monotone schemes are convergent to the weak (viscosity) solution but they are known to be at most first order accurate, whereas high-order schemes give a higher accuracy but in general are not stable. The crucial point is the coupling between the two schemes which is obtained via a *filter function* which selects which scheme has to be applied at a node of the grid in order to guarantee (under appropriate assumptions) a global convergence. The construction of these schemes is rather simple as explained by Oberman and Salvador [19] because one can couple various numerical methods and leave the filter function decide the switch between the two schemes. A general convergence result has been proved by Bokanowski, Falcone and Sahu in [5] and recently improved by Falcone, Paolucci and Tozza [11] with an adaptive and automatic choice of the parameter governing the switch. Note that the adaptation of the parameter depends on some regularity indicators in every cell, these indicators are computed at every iteration and this guarantees convergence.

Our contribution here is to construct a modified level-set approach for the segmentation problem where the velocity is slightly modified with respect to the standard velocity in order to have a regular evolution (see the details in Section 2) and to benefit of the high-order accuracy of the filtered scheme. Moreover, we apply the filtered scheme to the segmentation problem in two dimensions and we give some hints on how it should be implemented to take into account efficiently the modified velocity (Section 4). For readers convenience a short presentation of the filtered scheme is contained in Section 3 (more details and the convergence result are given in [12, 11]). The performances of this new method for the segmentation problem are illustrated in Section 5 where we compare it with a classical monotone scheme (first order accurate) on several virtual and real images presenting a detailed error analysis of the numerical results.

2 Image segmentation via a modified LS method

The key idea behind the use of the LS technique for the image segmentation problem is that the boundaries of one (or more) object(s) inside a given image are characterized by an abrupt change of the intensity values $I(x, y)$ of the image, so that the magnitude of $|\nabla I(x, y)|$ can be used as an indication of the edges. In this context, the definition of the velocity $c(x, y)$ in (1) plays an important role and must be defined in a proper way, close to 0 when the front is close to an edge, since the evolution should stop. The velocity will be positive or negative depending on the case, expanding or shrinking, respectively, without the possibility to change sign during the evolution.

Several *possible definitions of the velocity function* $c(x, y)$ has been proposed in literature. Typical examples are the following:

$$c_1(x, y) = \frac{1}{(1 + |\nabla(G * I(x, y))|^\mu)}, \quad \mu \geq 1, \quad (4)$$

where μ is used to give more weight to the changes in the gradient, if necessary. This function has been proposed in [8] with $\mu = 2$, and in [18] with $\mu = 1$. According to this definition, the velocity takes values in $[0, 1]$ and has values that are closer to zero in regions of high image gradient and values that are closer to unity in regions with relatively constant intensity.

Another possible choice, defined in [18], has the form

$$c_2(x, y) = 1 - \frac{|\nabla(G * I(x, y))| - M_2}{M_1 - M_2}, \quad (5)$$

where M_1 and M_2 are the maximum and minimum values of $|\nabla(G * I(x, y))|$. This latter velocity has similar properties with respect to the previous one, having values in $[0, 1]$ and being close

to 0 if the magnitude of the image gradient is close to its maximal value, and basically equal to 1 otherwise. It is clear that both definitions have the desired properties, but with slightly different features. More precisely, in the first case the velocity depends more heavily on the changes in the magnitude of the gradient, thus giving an easier detection of the edges but also possibly producing false edges inside the object (e.g. in presence of specular effects). On the other hand, the latter velocity is smoother inside the objects, being less dependent on the relative changes in the gradient, but might present some problems in the detection of all the edges if at least one of those is “more marked”.

2.1 Extension of the velocity function

As observed also in [18], the edge-stopping function (defined choosing one of the possible velocities previously introduced), has meaning only on the front Γ_t , since it was designed precisely to force the 0-level set to stop in the proximity of an edge. Consequently, it derives its meaning not from the geometry of v but only from the configuration of the front Γ_t . Using one of the classical velocity functions introduced before, as will be more clear from the numerical tests in Sect. 5 (especially the first one concerning a synthetic rhombus), high-order schemes produce unstable results since the representative function v produces oscillations near the edges where the front should stop. This problem can be solved by adding a limiter [5]. Here, we are interested in avoid the use of any limiter still producing stable results. That is why we need to extend the image-based velocity function $c(x, y)$ to all the level sets of the representation v in order to give a physical motivation also to the speed used to make all the other (infinite) level sets evolve.

In that spirit, we follow the idea discussed in [18], proposing a new and simple way to extend the velocity function which depends only on the initial condition v_0 and allows to avoid all the heavy computations required by the first solution proposed by the authors in [18], still obtaining stable results. Thus, recalling their approach, the first property that the velocity has to satisfy is:

Property 2.1. *Any external (image-based) speed function that is used in the equation of motion written for the function v should not cause the level sets to collide and cross each other during the evolutionary process.*

As we previously said, the appropriate extension depends on the choice of the initial representation. To present the basic idea, let us consider the distance (to the initial 0-level set) function, that is

$$v_0(x, y) = \text{dist} \{ (x, y), \Gamma_0 \}. \quad (6)$$

Therefore, with this choice we can define the velocity extension as follows:

Property 2.2. *The value of the speed function $c(x, y)$ at a point P lying on a level set $\{v = C\}$ is exactly the value of $c(x, y)$ at a point Q , such that the point Q is a distance C away from P and lies on the level set $\{v = 0\}$.*

Note that the point Q is uniquely determined whenever the normal direction in P is well defined. In fact, $Q = P - c(x, y)\eta(P)$, where η is the outgoing normal.

In order to apply this construction, in [18] the authors propose a simple but heavy procedure to track the point Q on the 0-level set associated to each point P of any level set. These computations clearly lead to the necessity of some modifications, such as the reinitialization for stability purposes and the *narrow band* approach to reduce the computational cost.

In this work, we avoid such problems in tracking the 0-level set, making use of the knowledge on the evolution and on the initial condition. The idea is straightforward and it is based on the fact that the evolution is oriented in the normal direction to the front. Whence, if the reciprocal disposition of the level sets is also known (that is why we must choose wisely the initial condition) and we make all the points in the normal direction to the 0-level set evolve

according to the same law, then it is reasonable to expect that all such points will keep their relative distance unchanged as time flows.

In order to present our modification, let us still consider the distance to Γ_0 (6) as initial condition. Then, by construction, all the C -level set are at a distance C from the 0-level set, as stated by Property 2.2. Hence, if we consider a generic point (x_c, y_c) on a C -level set, then it is reasonable to assume that the closest point on Γ_0 should be

$$(x_0, y_0) = (x_c, y_c) - v(t, x_c, y_c) \frac{\nabla v(t, x_c, y_c)}{|\nabla v(t, x_c, y_c)|}. \quad (7)$$

Therefore, it seems natural to define the extended velocity $\tilde{c}(x, y)$ as

$$\tilde{c}(x, y, v, v_x, v_y) = c \left(x - v \frac{v_x}{|\nabla v|}, y - v \frac{v_y}{|\nabla v|} \right), \quad (8)$$

which coincides with $c(x, y)$ on the 0-level set, as it is needed. The same approach can be applied as long as the initial distance between the level sets is known. In that case, if we want higher regularity to the evolving surface, which would be preferable in the case of high-order schemes such as the Adaptive Filtered scheme that we use in the numerical tests, we can define an appropriate initial condition, for example, by simply rotating a regular function in one space dimension. More precisely, let us consider a regular function $\bar{v}_0 : \mathbb{R}^+ \rightarrow \mathbb{R}$ such that $\bar{v}_0(r_0) = 0$, where r_0 is the radius of the initial circle Γ_0 (e.g. the right branch of a parabola centered in the origin), and let us define $v_0(x, y)$ rotating its profile, that is

$$v_0(x, y) = \bar{v}_0 \left(\sqrt{x^2 + y^2} \right). \quad (9)$$

Then, it is clear that the C -level set of v_0 are located at a distance

$$d(C) := \bar{v}_0^{-1}(C) - r_0, \quad \text{with } \bar{v}_0^{-1}(C) \geq 0, \quad (10)$$

from the 0-level set and, according to our previous remarks, they should keep this property as time evolves. Consequently, also in this case we can define

$$\tilde{c}(x, y, v, v_x, v_y) = c \left(x - d(v) \frac{v_x}{|\nabla v|}, y - d(v) \frac{v_y}{|\nabla v|} \right). \quad (11)$$

More details on the function $d(v)$ will be given in the next Section 2.2. For simplicity, in the last construction we assumed the representation function to be centered in the origin, but it is straightforward to extend the same procedure to more general situations. Note also that if we have only one object to be segmented (or we are considering the shrinking from the frame of the picture) we can always use a representation function centered in the origin since we can freely choose the domain of integration, given by the pixels of the image.

2.2 Motivations of the new velocity function

Since the idea behind the modification of the velocity $c(x, y)$ into $\tilde{c}(x, y, v, v_x, v_y)$ defined in (11) with $d(v) = 0$ if $v = 0$, is to follow the evolution of the 0-level set and then to define the evolution on the other level sets accordingly, we can see the new definition as a *characteristic based velocity*. Consequently, in order to justify our approach, as a first step we analyze the characteristics of the equation, assuming the regularity necessary for the computations. Therefore, we have to assume $v \in C^2(\Omega)$ (or at least C^2 in space and C^1 in time) and $c(x, y) \in C^1(\Omega)$, although the original problem does not satisfy (in general) these requirements. Let us assume that the characteristics do not cross each other during the evolution.

In order to simplify the presentation, we introduce the notations of the vectors $z := (x, y)$ and $p := (p_1, p_2) = (v_x, v_y)$. We will use these notations only in this section. Afterwards, the

gradient will be denoted by the usual notation (p, q) .

With these vectorial notations, the Hamiltonian in our case will be

$$H(z, v, p) = \tilde{c}(z, v, p)|p|. \quad (12)$$

Let us introduce the method of characteristics, writing the usual system

$$\begin{cases} \dot{z}(s) = \nabla_p H \\ \dot{v}(s) = \nabla_p H \cdot p - H \\ \dot{p}(s) = -\nabla H - H_v p, \end{cases} \quad (13)$$

where $\dot{\cdot}$ denotes the derivative with respect to the variable s . In our case, defining for brevity the point $(\xi, \zeta) := (x - d(v)\frac{p_1}{|p|}, y - d(v)\frac{p_2}{|p|})$, we compute

$$\begin{aligned} \frac{\partial H}{\partial p_1} &= \frac{\partial \tilde{c}}{\partial p_1} |p| + \tilde{c} \frac{\partial |p|}{\partial p_1} \\ &= \left(\frac{\partial c}{\partial \xi} \cdot \frac{\partial \xi}{\partial p_1} + \frac{\partial c}{\partial \zeta} \cdot \frac{\partial \zeta}{\partial p_1} \right) |p| + \tilde{c} \frac{\partial p_1}{\partial |p|} \\ &= -d(v) \frac{\partial c}{\partial \xi} \left(\frac{|p| - \frac{p_1^2}{|p|}}{|p|^2} \right) |p| - d(v) \frac{\partial c}{\partial \zeta} \left(-\frac{p_1 p_2}{|p|^3} \right) |p| + \tilde{c} \frac{p_1}{|p|} \\ &= -d(v) \frac{\partial c}{\partial \xi} \frac{p_2^2}{|p|^2} + d(v) \frac{\partial c}{\partial \zeta} \frac{p_1 p_2}{|p|^2} + \tilde{c} \frac{p_1}{|p|}, \end{aligned} \quad (14)$$

and analogously $\frac{\partial H}{\partial p_2}$, so that we obtain

$$\nabla_p H = \left(\begin{array}{c} \frac{d(v)p_2}{|p|^2} \left(p_1 \frac{\partial c}{\partial \zeta} - p_2 \frac{\partial c}{\partial \xi} \right) + \tilde{c} \frac{p_1}{|p|} \\ \frac{d(v)p_1}{|p|^2} \left(p_2 \frac{\partial c}{\partial \xi} - p_1 \frac{\partial c}{\partial \zeta} \right) + \tilde{c} \frac{p_2}{|p|} \end{array} \right) \Rightarrow \nabla_p H \cdot p = \tilde{c}(z, v, p)|p|. \quad (15)$$

Therefore, the system (13) becomes in our case the following:

$$\begin{cases} \dot{z}(s) = \nabla_p H \\ \dot{v}(s) = \tilde{c}(z, v, p)|p| - \tilde{c}(z, v, p)|p| = 0 \\ \dot{p}(s) = -\nabla \tilde{c}(z, v, p)|p| + d'(v) \nabla \tilde{c}(z, v, p)|p|^2 = \nabla \tilde{c}(z, v, p)|p|(d'(v)|p| - 1). \end{cases} \quad (16)$$

Now, if we define $d(v)$ such that

$$d'(v) = |p|^{-1}, \quad (17)$$

we have the final system

$$\begin{cases} \dot{z}(s) = \nabla_p H, \\ \dot{v}(s) = 0, \\ \dot{p}(s) = 0, \end{cases} \quad (18)$$

which states that, as long as the function \tilde{c} remains smooth enough ($\frac{\partial c}{\partial \xi} \approx 0$ and $\frac{\partial c}{\partial \zeta} \approx 0$), the characteristics are basically directed in the normal direction and along them both the height and the gradient are preserved. These last two properties are still valid when \tilde{c} is no longer smooth. Looking at the third relation of (18) and at the definition (17), since $p(s) \equiv p(0) = \nabla v_0$ along the characteristics, we can choose simply

$$d'(v) = |\nabla v_0|^{-1}, \quad (19)$$

which is the trivial case with the function $d(v) = v$ and also for $d(v)$ given by the previous definition (10). In fact, using the inverse function theorem, we have

$$d'(v) = \frac{d}{dv} (\bar{v}_0^{-1}(v)) = \frac{1}{\bar{v}'_0(w)}, \quad (20)$$

with w such that $\bar{v}_0(w) = v$. Moreover, recalling the definition (9), we can compute

$$\begin{aligned} |\nabla v_0(x, y)| &= \left| \nabla \bar{v}_0 \left(\sqrt{x^2 + y^2} \right) \right| \\ &= \left| \left(\frac{\bar{v}'_0 \left(\sqrt{x^2 + y^2} \right) x}{\sqrt{x^2 + y^2}}, \frac{\bar{v}'_0 \left(\sqrt{x^2 + y^2} \right) y}{\sqrt{x^2 + y^2}} \right) \right| \\ &= \frac{\bar{v}'_0 \left(\sqrt{x^2 + y^2} \right)}{\sqrt{x^2 + y^2}} \sqrt{x^2 + y^2} = \bar{v}'_0 \left(\sqrt{x^2 + y^2} \right), \end{aligned} \quad (21)$$

and then it is enough to consider (x, y) such that $w = \sqrt{x^2 + y^2}$.

Remark 2.3. *From a numerical point of view, the equations (17)-(19) give two different ways to compute the velocity at each time step. If we prefer to compute the function $d(v)$ analytically, through the knowledge of the initial condition v_0 , we have to use (19), whereas if we prefer to compute $d(v)$ independently on v_0 we can use, for example, a numerical integration for*

$$d(v) = \int \frac{1}{|\nabla v|} dx, \quad (22)$$

where the integral is taken on the projected characteristic $z(s)$. The latter choice would probably produce an even more stable scheme, assuming to be able to compute an accurate approximation of (22).

Thanks to the previous computations, we reached a good understanding of the nature of the evolution given by (1)-(11), but we still have not justified the main motivation that led us to define (11), that is to make all the level sets of v evolve according to the same law. More precisely, we have to show that, if we consider the evolution of two points on the same characteristic but on two different level sets, say the 0-level set $z^0(s)$ and a generic level set $z^\ell(s)$, then their relative distance (along the characteristic) does not change during the evolution. This fact would imply that, if we choose the level sets of v_0 to be such that

$$z^0(0) = z^\ell(0) - d(v_0) \frac{\nabla v_0}{|\nabla v_0|}, \quad (23)$$

than the points $\underline{z}(s) = z^\ell(s) - d(v) \frac{p}{|p|}$ are always on the 0-level set of v . In order to prove this last statement, let us proceed by a simple differentiation

$$\begin{aligned} \dot{\underline{z}}(s) &= \dot{z}^\ell(s) - \frac{d}{ds} \left(d(v) \frac{p}{|p|} \right) \\ &= \dot{z}^\ell(s) - \left[d'(v) \dot{v}(s) \frac{p}{|p|} + \frac{d(v)}{|p|^2} \left(\dot{p}(s) |p| - \frac{d}{ds} (|p(s)|) p \right) \right]. \end{aligned} \quad (24)$$

Recalling the relations in the system (18) with respect to $\dot{v}(s)$ and $\dot{p}(s)$, we can write

$$\begin{aligned} \dot{\underline{z}}(s) &= \dot{z}^\ell(s) + \frac{d(v)}{|p|^2} \left(\frac{p \cdot \dot{p}(s)}{|p|} \right) p \\ &= \dot{z}^\ell(s). \end{aligned} \quad (25)$$

This last computation states that all the level sets evolve according to the same law along characteristics. As a consequence, if (23) holds then $\underline{z}(s) \equiv z^0(s)$ till the characteristics do not cross, as we wanted.

One of the main consequences of this property, which will be very useful in the numerical implementation, is that the points $\left(z - d(v) \frac{\nabla v}{|\nabla v|} \right)$ are on the 0-level set of v as long as the

gradient is preserved. Then, assuming to have a coherent way to recover the point on the associated characteristic, we can approximate the problem by previously computing the points $\underline{z} = \left(z - d(v) \frac{\nabla v}{|\nabla v|} \right)$ and then updating the solution considering the *simplified problem* with (locally in time) *isotropic velocity*

$$v_t + c(\underline{z})|\nabla v| = 0, \quad (t, x, y) \in (t^n, t^{n+1}) \times \mathbb{R}^2. \quad (26)$$

This can be done in a very simple and direct manner, with only a slight increase in the computational cost, as we will see in Section 5. Otherwise, we should consider the full problem (1)-(11) and treat numerically all the dependence of $H(z, v, p)$.

3 The Adaptive Filtered Scheme

In this section we will introduce and illustrate the adaptive “filtered” (AF) scheme we will use to approximate the viscosity solution of the problem (1). For more details on the AF scheme, see [12]. We assume that the hamiltonian H and the initial data v_0 are Lipschitz continuous functions in order to ensure the existence and uniqueness of the viscosity solution [10]. For a detailed presentation of uniqueness and existence results for viscosity solutions, we refer the reader to [10] and [4].

Now, let us define a uniform grid in space $(x_j, y_i) = (j\Delta x, i\Delta y)$, $j, i \in \mathbb{Z}$, and in time $t_n = t_0 + n\Delta t$, $n \in [0, N_T]$, with $(N_T - 1)\Delta t < T \leq N_T\Delta t$. Then, we compute the numerical approximation $u_{i,j}^{n+1} = u(t_{n+1}, x_j, y_i)$ with the simple formula

$$u_{i,j}^{n+1} = S^{AF}(u^n)_{i,j} := S^M(u^n)_{i,j} + \phi_{i,j}^n \varepsilon^n \Delta t F \left(\frac{S^A(u^n)_{i,j} - S^M(u^n)_{i,j}}{\varepsilon^n \Delta t} \right), \quad (27)$$

where S^M and S^A are respectively the monotone and the high-order scheme dependent on both space variables, $F: \mathbb{R} \rightarrow \mathbb{R}$ is the *filter function* needed to switch between the two schemes, ε^n is the switching parameter at time t_n , and $\phi_{i,j}^n$ is the *smoothness indicator function* at the node (x_j, y_i) and time t_n , based on the 2D-smoothness indicators defined in [23]. The AF scheme here introduced is convergent, as proven in [11].

The two scheme composing the AF scheme can be freely chosen, provided that they satisfy the following assumptions:

Assumptions on S^M : The scheme is consistent, monotone and can be written in *differenced form*

$$u_{i,j}^{n+1} = S^M(u^n)_{i,j} := u_{i,j}^n - \Delta t h^M(x_j, y_i, D_x^- u_{i,j}^n, D_x^+ u_{i,j}^n, D_y^- u_{i,j}^n, D_y^+ u_{i,j}^n) \quad (28)$$

for a Lipschitz continuous function $h^M(x, y, p^-, p^+, q^-, q^+)$, with $D_x^\pm u_{i,j}^n := \pm \frac{u_{i,j\pm 1}^n - u_{i,j}^n}{\Delta x}$ and $D_y^\pm u_{i,j}^n := \pm \frac{u_{i\pm 1,j}^n - u_{i,j}^n}{\Delta y}$.

Assumptions on S^A : The scheme has a high-order consistency and can be written in *differenced form*

$$u_{i,j}^{n+1} = S^A(u^n)_{i,j} := u_{i,j}^n - \Delta t h^A \left(x_j, y_i, D_{k,x}^- u_{i,j}^n, \dots, D_x^- u_{i,j}^n, D_x^+ u_{i,j}^n, \dots, D_{k,x}^+ u_{i,j}^n, \right. \\ \left. D_{k,y}^- u_{i,j}^n, \dots, D_y^- u_{i,j}^n, D_y^+ u_{i,j}^n, \dots, D_{k,y}^+ u_{i,j}^n \right), \quad (29)$$

for a Lipschitz continuous function $h^A(x, y, p^-, p^+, q^-, q^+)$ (in short), with $D_{k,x}^\pm u_{i,j}^n := \pm \frac{u_{i,j\pm k}^n - u_{i,j}^n}{k\Delta x}$ and $D_{k,y}^\pm u_{i,j}^n := \pm \frac{u_{i\pm k,j}^n - u_{i,j}^n}{k\Delta y}$.

Example 3.1. As examples of monotone schemes in differenced form satisfying the hypotheses stated before, we can consider the simple numerical hamiltonian

$$h^M(p^-, p^+, q^-, q^+) := \sqrt{\max\{p^-, -p^+, 0\}^2 + \max\{q^-, -q^+, 0\}^2} \quad (30)$$

for the eikonal equation

$$v_t + \sqrt{v_x^2 + v_y^2} = 0, \quad (31)$$

or, for more general equations also depending on the space variables, we can use the 2D-version of the local Lax-Friedrichs hamiltonian

$$h^M(x, y, p^-, p^+, q^-, q^+) := H\left(x, y, \frac{p^+ + p^-}{2}, \frac{q^+ + q^-}{2}\right) - \frac{\alpha_x(p^-, p^+)}{2}(p^+ - p^-) - \frac{\alpha_y(q^-, q^+)}{2}(q^+ - q^-), \quad (32)$$

with

$$\alpha_x(p^-, p^+) := \max_{\substack{x, y, q, \\ p \in I(p^-, p^+)}} |H_p(x, y, p, q)|, \quad \alpha_y(q^-, q^+) := \max_{\substack{x, y, p, \\ q \in I(q^-, q^+)}} |H_q(x, y, p, q)|, \quad (33)$$

where $I(a, b) := [\min(a, b), \max(a, b)]$. This scheme is monotone under the restrictions $\frac{\Delta t}{\Delta x} \cdot \alpha_x + \frac{\Delta t}{\Delta y} \cdot \alpha_y \leq 1$.

Example 3.2. An example of numerical hamiltonian h^A satisfying the assumptions required is the Lax-Wendroff hamiltonian

$$h^A(x, y, D_x^\pm u, D_y^\pm u) := H(x, y, D_x u, D_y u) - \frac{\Delta t}{2} [H_p(x, y, D_x u, D_y u) (H_p(x, y, D_x u, D_y u) D_x^2 u + H_x(x, y, D_x u, D_y u)) + H_q(x, y, D_x u, D_y u) (H_q(x, y, D_x u, D_y u) D_y^2 u + H_y(x, y, D_x u, D_y u)) + 2H_p(x, y, D_x u, D_y u) H_q(x, y, D_x u, D_y u) D_{xy}^2 u], \quad (34)$$

where $D_x^\pm u, D_x u, D_x^2 u$ are, respectively, the usual one-sided and centered one-dimensional finite difference approximations of the first and second derivative in the x -direction (analogously for the y -direction), whereas for the mixed derivative we use

$$D_{xy}^2 u_{i,j} := \frac{u_{i+1,j+1} - u_{i-1,j+1} - u_{i+1,j-1} + u_{i-1,j-1}}{4\Delta x \Delta y}. \quad (35)$$

Note that the derivatives of H can be computed either analytically or by some second order numerical approximation. In particular, to compute the derivative H_x , we can simply use

$$(H_x)_{i,j} := \frac{H(x_{j+1}, y_i, D_x u_{i,j}, D_y u_{i,j}) - H(x_{j-1}, y_i, D_x u_{i,j}, D_y u_{i,j})}{2\Delta x}, \quad (36)$$

and analogously for H_y .

For more details on the construction of S^M and S^A and other examples of possible numerical hamiltonians, see [23, 11].

In our approach, in order to couple the two schemes, we need to define three key quantities:

1. The *filter function* F , which must satisfy

- (a) $F(r) \approx r$ for $|r| \leq 1$ so that if $|S^A - S^M| \leq \Delta t \varepsilon^n$ and $\phi_{i,j}^n = 1 \Rightarrow S^{AF} \approx S^A$,
- (b) $F(r) = 0$ for $|r| > 1$ so that if $|S^A - S^M| > \Delta t \varepsilon^n$ or $\phi_{i,j}^n = 0 \Rightarrow S^{AF} = S^M$.

Several choices for F are possible, different for regularity properties. In this paper, we will consider the discontinuous filter already used in [5] and defined as follows:

$$F(r) := \begin{cases} r & \text{if } |r| \leq 1 \\ 0 & \text{otherwise,} \end{cases} \quad (37)$$

which is clearly discontinuous at $r = -1, 1$ and satisfies trivially the two required properties.

2. If we want the scheme (27) to switch to the high-order scheme when some regularity is detected, we have to choose ε^n such that

$$\left| \frac{S^A(v^n)_{i,j} - S^M(v^n)_{i,j}}{\varepsilon^n \Delta t} \right| = \left| \frac{h^A(\cdot, \cdot) - h^M(\cdot, \cdot)}{\varepsilon^n} \right| \leq 1, \quad \text{for } (\Delta t, \Delta x, \Delta y) \rightarrow 0, \quad (38)$$

in the *region of regularity at time t_n* , that is

$$\mathcal{R}^n := \{(x_j, y_i) : \phi_{i,j}^n = 1\}. \quad (39)$$

Proceeding by Taylor expansion for the monotone and the high-order hamiltonians, by (38) we arrive to a lower bound for ε^n . The simplest numerical approximation of that lower bound is the following

$$\varepsilon^n = \max_{(x_j, y_i) \in \mathcal{R}^n} K \left| \frac{\Delta t}{2} [H_p (H_x + H_p D_x^2 u^n) + H_q (H_y + H_q D_y^2 u^n) + 2H_p H_q D_{xy}^2 u^n] + \left(\tilde{h}_{p^+}^M - \tilde{h}_{p^-}^M \right) + \left(\tilde{h}_{q^+}^M - \tilde{h}_{q^-}^M \right) \right|, \quad (40)$$

in which we have used the usual notation for the gradient, i.e. $(p, q) := (v_x, v_y)$ and

$$\tilde{h}_{p^+}^M := h^M(x, y, D_x u^n, D_x^+ u^n, D_y u^n, D_y u^n) - h^M(x, y, D_x u^n, D_x^- u^n, D_y u^n, D_y u^n). \quad (41)$$

The definition of $\tilde{h}_{p^-}^M, \tilde{h}_{q^+}^M, \tilde{h}_{q^-}^M$ follows from (41) in an analogous way. All the derivatives of H are computed at $(x, y, D_x u^n, D_y u^n)$ and the finite difference approximations around the point (i, j) , using $K > \frac{1}{2}$. See [23] for more details.

3. For the definition of a function ϕ , needed to detect the region \mathcal{R}^n , we require

$$\phi_{i,j}^n := \begin{cases} 1 & \text{if the solution } u^n \text{ is regular in } I_{i,j}, \\ 0 & \text{if } I_{i,j} \text{ contains a point of singularity,} \end{cases} \quad (42)$$

with $I_{i,j} := [x_{j-1}, x_{j+1}] \times [y_{i-1}, y_{i+1}]$. In order to proceed with the construction, we split the cell $I_{i,j}$ into four subcells, denoted by the superscript ' $\vartheta_1 \vartheta_2$ ', for $\vartheta_1, \vartheta_2 = +, -$, according to the shift with respect to the center (x_j, y_i) . Then, we measure the regularity of the solution inside each subcell by first computing the *smoothness coefficients*

$$\beta_k^{\vartheta_1 \vartheta_2} = \frac{1}{\Delta x \Delta y} \left[u_{[3,1]}^2 + u_{[1,3]}^2 + u_{[2,2]}^2 + \frac{17}{12} (u_{[3,2]}^2 + u_{[2,3]}^2) + \frac{317}{720} u_{[3,3]}^2 + u_{[3,1]} u_{[3,2]} + u_{[1,3]} u_{[2,3]} - \frac{1}{6} (u_{[3,1]} u_{[3,3]} + u_{[1,3]} u_{[3,3]}) - \frac{1}{12} (u_{[3,2]} u_{[3,3]} + u_{[2,3]} u_{[3,3]}) \right] \quad (43)$$

for $k = 0, 1$, where we have dropped the dependence on the time step t^n for brevity and we have used the shorter notation $u_{[t,s]}$ to denote the multivariate undivided difference of u of order t in x and s in y . Note that the previous formula can be used to obtain all the needed quantities as long as the following *ordered stencils* are used to compute the undivided differences

- $\mathcal{S}_0^- = \{x_{j-1}, x_j, x_{j+1}\} \times \{y_{i-1}, y_i, y_{i+1}\}$, $\mathcal{S}_1^- = \{x_j, x_{j-1}, x_{j-2}\} \times \{y_i, y_{i-1}, y_{i-2}\}$;
- $\mathcal{S}_0^+ = \{x_{j+1}, x_j, x_{j-1}\} \times \{y_{i-1}, y_i, y_{i+1}\}$, $\mathcal{S}_1^+ = \{x_j, x_{j+1}, x_{j+2}\} \times \{y_i, y_{i-1}, y_{i-2}\}$;
- $\mathcal{S}_0^{++} = \{x_{j+1}, x_j, x_{j-1}\} \times \{y_{i+1}, y_i, y_{i-1}\}$, $\mathcal{S}_1^{++} = \{x_j, x_{j+1}, x_{j+2}\} \times \{y_i, y_{i+1}, y_{i+2}\}$;
- $\mathcal{S}_0^{-+} = \{x_{j-1}, x_j, x_{j+1}\} \times \{y_{i+1}, y_i, y_{i-1}\}$, $\mathcal{S}_1^{-+} = \{x_j, x_{j-1}, x_{j-2}\} \times \{y_i, y_{i+1}, y_{i+2}\}$.

Since these coefficients are such that

- $\beta_k = O(\Delta x^2 + \Delta x \Delta y + \Delta y^2)$ if the solution is smooth in \mathcal{S}_k ;
- $\beta_k = O(1)$ if there is a singularity in \mathcal{S}_k ,

according to the usual WENO procedure we weight the obtained information and focus on the ‘inner’ stencil, denoted by the subscript ‘0’, by computing

$$\omega^{\vartheta_1 \vartheta_2} = \frac{\alpha_0^{\vartheta_1 \vartheta_2}}{\alpha_0^{\vartheta_1 \vartheta_2} + \alpha_1^{\vartheta_1 \vartheta_2}}, \quad (44)$$

where $\alpha_k^{\vartheta_1 \vartheta_2} = \frac{1}{(\beta_k^{\vartheta_1 \vartheta_2} + \sigma_h)^2}$, with $\sigma_h = h_x^2 + h_y^2$, which represents the measure of smoothness of the solution in each subcell. Once we have computed the four indicators, we couple the information by defining

$$\omega = \min\{\omega^{--}, \omega^{+-}, \omega^{-+}, \omega^{++}\}. \quad (45)$$

At this point, in order to reduce spurious oscillations in regular regions, we use the *mapping* first introduced in [14] to propose a modification of the original WENO procedure, called *M-WENO*, that is

$$\omega^* = g(\omega) = 4\omega \left(\frac{3}{4} - \frac{3}{2}\omega + \omega^2 \right). \quad (46)$$

Finally, in order to define our function ϕ , it is enough to take

$$\phi(\omega^*) = \chi_{\{\omega^* \geq M\}}, \quad (47)$$

with $M < \frac{1}{2}$ (e.g. $M = 0.1$ in the tests reported in Sect. 5), a number that can also depend on Δx and Δy . For more details and other possible constructions for the definition of ϕ , we refer the interested reader to [23, 11].

Remark 3.3. *Choosing $\varepsilon^n \equiv \varepsilon \Delta x$, with $\varepsilon > 0$ and $\phi_{i,j}^n \equiv 1$, we get the Filtered Scheme of [5], so here we are generalizing that approach to exploit more carefully the local regularity of the solution at every time t^n and cell $I_{i,j}$.*

4 Numerical implementation of the modified LS method

Before illustrating the numerical tests, let us first give some comments on the numerical schemes composing the AF scheme adopted for the tests in Sect. 5. The main issue concerning the *local Lax-Friedrichs* and the *Lax-Wendroff schemes* defined by (32) and (34), respectively, is the need to compute the one-directional velocities H_p and H_q which depend also on $\frac{\partial c}{\partial \xi}$ and $\frac{\partial c}{\partial \zeta}$, as visible in (15). Moreover, in order to implement the local Lax-Friedrichs scheme we should be able to compute the maximum of $|H_p|$ (resp. $|H_q|$) uniformly with respect to p (resp. q), which is a very intricate matter due to the (possible) low regularity of \tilde{c} . In fact, if we focus on the usual behavior of $c(x, y)$ in the proximity of a relevant edge, we can expect the derivatives $\frac{\partial c}{\partial \xi}$ and $\frac{\partial c}{\partial \zeta}$ to be really big. This is not surprising since the front decelerates rapidly in the neighborhood of an edge. In addition, in order to solve the full model (1)-(11), we should take into account also the remaining dependence of $H(x, y, v, \cdot, \cdot)$ when deriving the second-order Lax-Wendroff scheme and, clearly, the formula to compute the threshold ε^n . Finally, concerning the CFL condition, it is necessary to compute $\max\{|H_p|, |H_q|\}$ with the full formula (15). Consequently, λ could be excessively small due to the low regularity of \tilde{c} . In this latter case, we would clearly need an adaptive mesh refinement technique to reduce the computational cost.

In order to avoid most of these complications in the numerical implementation, we choose to approximate the solution of the simplified problem (26), adjusting the velocity \tilde{c} according to (11) at each time step. Using the simplified problem (26), we can use the simple relation

$$\max_p \max_q |H_p(\cdot, p, q)| = \max_p |H_p(\cdot, p, 0)|, \quad (48)$$

avoiding to take the maximums over all the possible values of p and q , which is instead required for the resolution of the full problem (1)-(11) with anisotropic velocity \tilde{c} . Analogous comment holds for H_q . Lastly, from the numerical point of view, the use of this simplification brings another fundamental consequence: when we apply the numerical schemes to solve (26), we are considering, formally, a problem with bounded velocities $\max\{|H_p|, |H_q|\} \leq 1$. This implies that we can choose the following CFL condition:

$$\lambda := \max \left\{ \frac{\Delta t}{\Delta x}, \frac{\Delta t}{\Delta y} \right\} \leq \frac{1}{2} \max\{|H_p|^{-1}, |H_q|^{-1}\}, \quad (49)$$

using the relation (48), which is a less restrictive condition with respect to the original one coming from the full problem (1)-(11).

In the following, we will use the same notations introduced in Sect. 3, except for the number of time steps N_T , which will be replaced by the total number of iterations N_i used by the scheme, since now we are looking for an asymptotic solution (in some stationary sense). The maximum number of iterations, which is fixed at the beginning of the procedure, will be denoted by N_{\max} .

Let us give some details on the precise numerical implementation, commenting the main procedures involved in the (sketched) *Algorithm 1*.

Algorithm 1 Segmentation via the LS Method

Input: $\mu, K_{reg}, tol, N_{\max}, I, u_0$

$E^0 = 1, n = 0$

regularize the matrix I (apply the Gaussian filter)

compute the velocity matrix c using (4) or (5)

store the position of the front in the matrix F^0

while ($E^n \geq tol$) and ($n < N_{\max}$) **do**

 Step 1: compute the modified velocity matrix \tilde{c}^n using (11)

 Step 2: update the solution $u^n \rightarrow u^{n+1}$

$n = n + 1$

 Step 3: store the front F^n

 compute the error E^n

$N_i = n$

Output: N_i, u^{N_i} .

Let us set the parameters of the simulation, which are the power μ in (4), the number of iterations K_{reg} of the heat equation for the Gaussian filter, the tolerance $tol > 0$ of the stopping criterion, the amplitude of the pixels $(\Delta x, \Delta y)$ and, subsequently, the time step Δt according to the CFL condition (49).

Then, at each iteration $n = 0, \dots, N_i$, which has to be interpreted in the sense “until convergence” (note that N_i is not known a priori, but depends on the stopping criterion described in Step 3 and can be equal to N_{max} in case of not convergence of the scheme), we repeat the following steps.

Step 1. For $i = 0, \dots, N_y, j = 0, \dots, N_x$, with $(N_x + 1) \times (N_y + 1)$ the size of the input image, we precompute the matrix $\tilde{c}(x_j, y_i, u_{i,j}, D_x u_{i,j}, D_y u_{i,j})$ at the beginning of each iteration using central finite difference approximations for the first order derivatives $D_x u_{i,j}$ and $D_y u_{i,j}$. Note that the quantities only depend on (i, j) also through u . Clearly, this method is valid only as long as the representation function u remains smooth at all the level sets, and should be justified in the case of singular edges (although we will not pursue this precise matter). Moreover, in

general the point

$$(x_{j_u}, y_{i_u}) := \left(x_j - d(u_{i,j}) \frac{D_x u_{i,j}}{\sqrt{(D_x u_{i,j})^2 + (D_y u_{i,j})^2}}, y_i - d(u_{i,j}) \frac{D_y u_{i,j}}{\sqrt{(D_x u_{i,j})^2 + (D_y u_{i,j})^2}} \right) \quad (50)$$

is not a point of the grid (x_j, y_i) .

To reconstruct the correct value (or at least a reasonable approximation) we propose two different implementations. The first one is a simple *bilinear reconstruction* from the neighboring values

$$\mathcal{N}_u := \{(x_{\lfloor j_u \rfloor}, y_{\lfloor i_u \rfloor}), (x_{\lceil j_u \rceil}, y_{\lceil i_u \rceil}), (x_{\lfloor j_u \rfloor}, y_{\lceil i_u \rceil}), (x_{\lceil j_u \rceil}, y_{\lfloor i_u \rfloor})\}, \quad (51)$$

where we have used the notation

$$\lfloor j_u \rfloor := j - \left\lceil \frac{x_{j_u} - x_j}{\Delta x} \right\rceil \quad \text{and} \quad \lfloor i_u \rfloor := i - \left\lceil \frac{y_{i_u} - y_i}{\Delta y} \right\rceil, \quad (52)$$

with the other cases following an analogous definition. The second possibility, which we use in the numerical examples since it seems to give nicer results in terms of the shape of the approximate representation u , consists in taking as (x_{j_u}, y_{i_u}) the point such that

$$|u_{i_u, j_u}| := \min_{(x_j, y_i) \in \mathcal{N}_u} |u_{i,j}|. \quad (53)$$

Note that this construction is well defined only if $|\nabla u_{i,j}| \neq 0$. Therefore, we define the updated velocity matrix as

$$\tilde{c}_{i,j}^n := \begin{cases} c_{i_u, j_u} & \text{if } |\nabla u_{i,j}| \neq 0, \\ c_{i,j} & \text{otherwise,} \end{cases} \quad (54)$$

and we use \tilde{c}^n as an isotropic velocity in the next step.

Step 2. We approximate the problem (26) using the AF scheme (27), with the local Lax-Friedrichs scheme (32) as S^M and the Lax-Wendroff scheme (34) as S^A . From now on, we will refer to this AF implemented scheme with the acronym AF-LW.

We add homogeneous Neumann boundary conditions to the problem (26) in all our experiments in order to not alter the average intensity of the image.

Step 3. In this last step, we describe how approximating the front Γ_t . Since Γ_t is a curve, it is composed by points that are not all grid points belonging to our mesh. Hence, in order to approximate the position of the front at each time step t , we consider a neighborhood θ_δ of the front Γ_t of radius $\delta = \max\{\Delta x, \Delta y\}$. In this way, stopping the evolution as soon as the front ceases to move will be equivalent to require that the neighborhood θ_δ ceases to move. In order to apply that procedure, at each iteration n we store the values of the points (x_j, y_i) such that $u_{i,j}^n$ changes sign in a matrix $F_{i,j}^n$ (we use the closest points on the grid, that are $(i, j \pm 1)$ and $(i \pm 1, j)$), and set $F_{i,j}^n = 0$ otherwise. In this way we automatically store the disposition of the front with an error of order $\delta = \max\{\Delta x, \Delta y\}$, i.e. we approximate the position of the front, as desired.

We will continue to do that at each iteration until the matrix F at two consecutive iterations will be “close enough”. For this reason, we consider two stopping rules:

$$E_\infty := \|u^{n+1} - u^n\|_{L^\infty(\theta_\delta)} = \max_{i,j} |F_{i,j}^n - F_{i,j}^{n-1}| < \tau, \quad (55)$$

where $\tau > 0$ is the prescribed tolerance a priori chosen,

$$E_1 := \|u^{n+1} - u^n\|_{L^1(\theta_\delta)} = \Delta x \Delta y \sum_{i,j} |F_{i,j}^n - F_{i,j}^{n-1}| < \tau, \quad (56)$$

where now a dependence on the discretization parameters appears.

In our implementation we use one of the two *stopping rules* above introduced combined with a condition on the number of allowed iterations (i.e. $n < N_{max}$).

5 Numerical simulations

In this section we present a series of numerical experiments on both synthetic and real images, comparing the results obtained with the AF scheme and with the simple monotone scheme. The first aim is to show the possible improvements of the modified model with respect to the classical formulation. In fact, after extensive numerical simulations, we noticed that the classical model is not well defined when using high-order schemes, since they can produce heavy oscillations as soon as the Lipschitz constant of the representation function becomes too big. This effect causes the stopping rule to be practically ineffective (in both norms) in most cases tested when using the AF scheme, whereas the simple monotone scheme seems to give always stable results. Note that, when the singularity develops, the “neighborhood” of the front becomes more and more vertical as time flows, creating additional difficulties in tracking the 0-level set.

The numerical tests illustrated in this section will show the comparison of the results also varying the initial datum, when using the modified velocity, or varying the norm for the stopping rule defined in (55) and (56), when using the classical model. Moreover, in the case of synthetic tests, we also vary the space steps Δx and Δy , that we consider equal to each other ($\Delta x = \Delta y$), and, therefore, the total number of considered pixels.

Now, let us specify the initial condition used in each case. When the velocity is defined by the classical model, in the expansion case (*Case a*) we use the paraboloid

$$u_0(x, y) = \min \left\{ x^2 + y^2 - r^2, \frac{1}{2}r^2 \right\}, \quad (57)$$

where $r > 0$ is the radius of the initial circle and $\frac{1}{2}r^2$ a value chosen in order to cut the surface from above (therefore we have a flat surface at the numerical boundary), whereas in the shrinking case (*Case b*) we use the truncated pyramid (tent) with a square (rectangular) base, that is

$$u_0(x, y) = \min\{2(x - b_x), 2(a_x - x), 2(y - b_y), 2(a_y - y), -0.2\}, \quad (58)$$

where $[a_x, b_x] \times [a_y, b_y]$ is the frame of the image, -0.2 is the value at which we truncate the pyramid (tent) and 2 is the steepness of the faces of the surface (the smaller the value, the less steep the faces are). With this choice we use a slightly more regular front with respect to the discontinuous representation that simply changes value crossing the frame of the image, still being able to keep the whole surface outside the region occupied by the objects to segment.

On the other hand, when using the modified velocity \tilde{c} , in the expansion case (*Case a*) we consider two different initial data: the paraboloid as in (57) (*Datum 1*) or the following distance function (*Datum 2*)

$$u_0(x, y) = \text{dist}\{(x, y), \Gamma_0^1\}, \quad (59)$$

where Γ_0^1 is the usual circle centered in $(0, 0)$ with radius $r = 0.5$ unless otherwise stated. Instead, for the shrinking case (*Case b*) we only use the distance function

$$u_0(x, y) = \text{dist}\{(x, y), \Gamma_0^2\}, \quad (60)$$

with Γ_0^2 representing the frame of the image. We summarize the different initial conditions in Table 1.

In order to give a quantitative evaluation of the performances in addition to the qualitative analysis, in the reported tables we will compare the results in terms of *number of iterations* N_i and *relative error in pixels*, defined as

$$P\text{-Err}_{rel} = \frac{|P_{ex} - P_a|}{P_{ex}}, \quad (61)$$

where P_{ex} and P_a are the number of pixels inside the exact and approximated boundaries of the object(s), respectively. Note that we can compute the “exact” object only if the background is

Table 1: Summary of the initial conditions considered in the numerical tests.

	c	\tilde{c}
Expansion case (Case a)	u_0 as Paraboloid (57)	Datum 1: u_0 as Paraboloid (57) Datum 2: u_0 as Distance from Γ_0^1 (59)
Shrinking case (Case b)	u_0 as Truncated pyramid (or tent) (58)	u_0 as Distance from Γ_0^2 (60)

really smooth (in the synthetic cases it is always uniform), because we usually use a comparison with a “threshold” for the values of $I(x, y)$ in order to select the regions occupied by the object (exact object). Whereas, for the approximated object we will count the pixels for which $u_{i,j} \leq 0$. Moreover, we measure the error also with a closely related quantity, that is

$$P\text{-Err}_1 = |P_{ex} - P_a| \Delta x \Delta y, \quad (62)$$

in order to show some dependence on the discretization parameters.

If the schemes do not arrive to convergence in the fixed maximum number of allowed iterations N_{\max} , we will put a “–” inside the tables, in place of N_i . For all our tests, we will set $N_{\max} = 2000$. Moreover, in case the front does not stop correctly on the boundary of the object, thus giving an unstable and unusable result, we will put an “X” in correspondence of the errors column. For each test, we specify the main parameters involved (μ , K_{reg} , tol and $\Delta x = \Delta y$ or $\#Nodes$), the norm used in the stopping rule and the chosen velocity function. For all the numerical tests presented in this paper, we use CFL number $\lambda = \max \left\{ \frac{\Delta t}{\Delta x}, \frac{\Delta t}{\Delta y} \right\} = \frac{1}{2}$, $K = 1$ in the formula (40) for the computation of ε , and the velocity function c_1 defined in (4) for the classical model, referring to it simply as the classical c . All the numerical tests have been implemented in language C++, with plots and computation of the errors in MATLAB. The computer used for the simulations is a MacBook Pro 13” Intel Core 2 Duo with speed of 2.66 GHz and 4 GB of RAM.

5.1 Synthetic tests

Let us begin by presenting a simple synthetic example, in which we compare the performances of the filtered scheme and the monotone one using both velocities. The main aim here is to compare the behavior of the two schemes with respect to the use of the classical velocity c and the modified one \tilde{c} , and the performances varying the number of grid nodes.

5.1.1 Test 1. Rhombus

For this first test, we decided to perform the simulations only in the case of an expansion, since these situations are even more easily handled by a shrinking front and the results do not vary evidently changing the schemes or the velocity.

The rhombus considered is defined by the equation

$$\frac{|x|}{2} + |y| = \frac{3}{4}, \quad (x, y) \in [-2, 2]^2, \quad (63)$$

that produces a final front visible in Figure 1, which presents some heavily marked corners. This causes some serious problems when using the classical model at least if the filtered scheme is involved.

In fact, looking at Table 2, we can see that the AF-LW scheme achieves convergence, in the sense of the iterative stopping rule (55), but after having lost track of the boundary (the front overcomes the edge of the object and then keeps expanding). This happens also varying

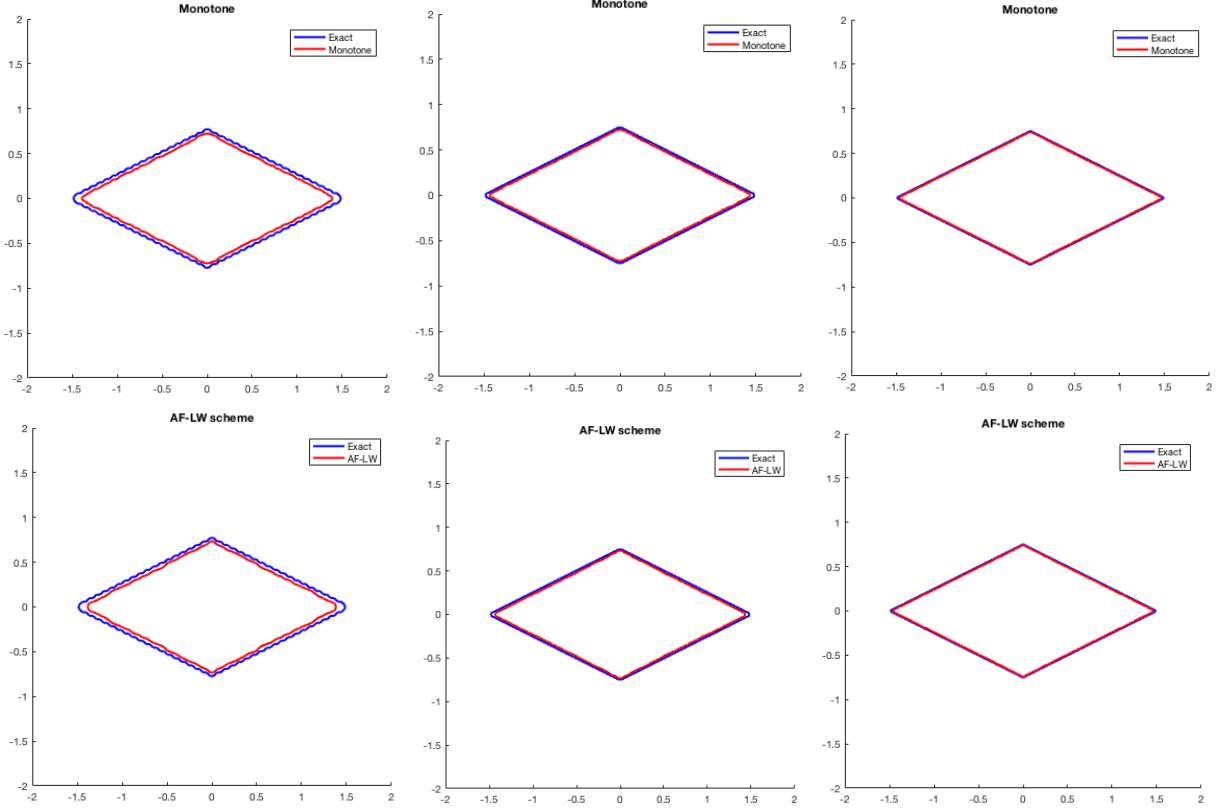


Figure 1: (Test 1a) Datum 1. Plots of the final front obtained by the Monotone scheme (top) and the AF-LW scheme (bottom) with the parameters used in Table 3.

the number of grid nodes (from 102 to 402). Regarding the monotone scheme, it converges, the two errors reported decrease by refining the grid with the decreasing of the space step Δx , considering the same parameters μ, K_{reg} and same tolerance tol . On the other hand, if we use the modified velocity \tilde{c} (see Table 3), the monotone scheme converges in a less number of iterations N_i and with lower errors with respect to the correspondent results obtained by using the classical velocity. For comparisons reasons, note that we used the same parameters, tolerance and initial datum (the paraboloid, Datum 1) for both velocities. The AF-LW scheme converges and give always better results in terms of both errors and number of iterations with respect to the monotone scheme with c or \tilde{c} . Hence, both schemes benefit of the new definition of velocity and the AF-LW scheme with \tilde{c} gives the best performances. Moreover, looking at Tab. 4 which contains the CPU times in seconds related to both schemes needed to obtain the results reported in Tab. 3, the AF-LW scheme need a longer time but it is always less than one minute. Hence, the best performances are reached in a very short time.

Table 2: (Test 1a) Errors and number of iterations varying $\#Nodes$.

c	Norm $\ \cdot \ _{\infty}$			Monotone			AF-LW		
	tol	μ	K_{reg}	N_i	$P-Err_{rel}$	$P-Err_1$	N_i	$P-Err_{rel}$	$P-Err_1$
102	0.0005	2	0	84	0.1025	0.2321	213	X	X
202	0.0005	2	0	152	0.0526	0.1172	394	X	X
402	0.0005	2	0	288	0.0265	0.0593	745	X	X

Table 3: (Test 1a) Errors and number of iterations varying $\#Nodes$ (L^∞ norm).

\tilde{c}	Datum 1			Monotone			AF-LW		
$\#Nodes$	tol	μ	K_{reg}	N_i	$P-Err_{rel}$	$P-Err_1$	N_i	$P-Err_{rel}$	$P-Err_1$
102	0.0005	2	0	50	0.0748	0.1694	48	0.0693	0.1568
202	0.0005	2	0	100	0.0427	0.0950	96	0.0363	0.0808
402	0.0005	2	0	199	0.0208	0.0466	196	0.0203	0.0454

Table 4: (Test 1a) CPU times in seconds related to the Tab. 3.

$\#Nodes$	Monotone	AF-LW
102	0.20	0.86
202	1.58	6.71
402	12.32	53.60

A more correct analysis can be made by decreasing the tolerance tol together with the number of nodes $\#Nodes$. This is what we have done and is visible in Tables 5 and 6. Analyzing the behaviors of the schemes with respect to the initial data, looking at Table 5 we can note that the monotone scheme is not influenced by the change of the initial datum in terms of number of iterations. In fact, comparing the two columns related to N_i , only one iteration in the last row is different. With respect to the errors, small changes are visible, with a small improvement using Datum 2 for the last two rows. Regarding the AF-LW scheme, from Table 6 we can see better performances with lower (or equal) errors and lower (or equal) N_i when using Datum 2. For both schemes, the errors decrease when we refine the grid. Comparing the two Tables 5 and 6, we can note that the AF-LW scheme get always better results in terms of number of iterations and errors with both initial data with respect to the monotone scheme, except for the last refinement ($\#Nodes = 402$) with Datum 2, in which the monotone scheme seems to be a little bit better, due to round off errors.

Table 5: (Test 1a) Errors and number of iterations varying $\#Nodes$ (L^∞ norm).

\tilde{c}	Monotone			Datum 1			Datum 2		
$\#Nodes$	tol	μ	K_{reg}	N_i	$P-Err_{rel}$	$P-Err_1$	N_i	$P-Err_{rel}$	$P-Err_1$
102	0.001	2	0	50	0.0748	0.1694	50	0.0776	0.1757
202	0.0005	2	0	100	0.0427	0.0950	100	0.0420	0.0935
402	0.00025	2	0	199	0.0208	0.0466	200	0.0199	0.0446

Table 6: (Test 1a) Errors and number of iterations varying $\#Nodes$ (L^∞ norm).

\tilde{c}	AF-LW			Datum 1			Datum 2		
$\#Nodes$	tol	μ	K_{reg}	N_i	$P-Err_{rel}$	$P-Err_1$	N_i	$P-Err_{rel}$	$P-Err_1$
102	0.001	2	0	48	0.0693	0.1568	47	0.0658	0.1490
202	0.0005	2	0	96	0.0363	0.0808	96	0.0363	0.0808
402	0.00025	2	0	196	0.0203	0.0454	195	0.0201	0.0450

5.2 Real tests

In this section we consider real images, with a particular attention to the biomedical ones. Thanks to the error formulas (61) and (62), we can provide a sort of quantitative evaluation of the performances of the schemes in addition to the qualitative one in terms of “pixels errors” (number of pixels composing the area of the objects to be segmented) also for the real tests.

5.2.1 Test 2. Brain

The first biomedical test focuses on a human brain (Input image size: 340×340 pixels). For this test, we approximate the relevant “external” boundary of the brain by an expansion (Case a) or a shrinking (Case b) of the front, so that we start from inside or outside as visible in Fig. 2.

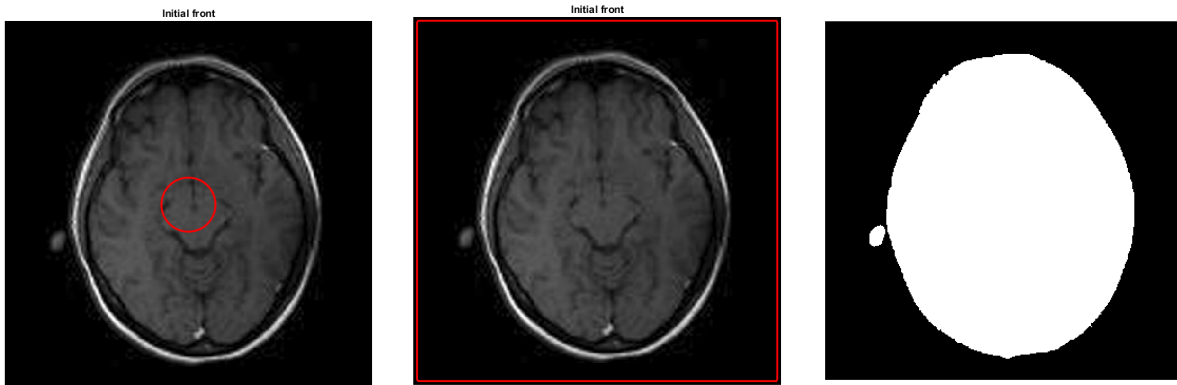


Figure 2: (Test 2) From left to right: Initial front for the expansion case (Case 2a) composed by a circle of radius $r = 0.25$; initial front for the shrinking case (Case 2b); mask used for the pixel errors in Case 2b.

Let us begin to analyze the results in the expansion case. Looking at Figs. 3 and 4, it is simple to note that the AF scheme recognizes better the boundary of the object starting from two different initial datum. Note that the first and third pictures reported in Figs. 3 and 4 show the results of the two schemes obtained with same parameters (included tol) and looking in the middle at the bottom of the two figures the differences are evident. In the picture reported in the middle for both figures 3 and 4, we show the results obtained by using the monotone scheme with a different and lower tol in order to show that in that case the monotone scheme can increase its resolution even if with a high number of iterations and in any case not better than the AF-LW scheme. In Case a, hence, the qualitative evaluation is enough to understand which scheme provides the better results. Instead, in the shrinking case, a quantitative error evaluation is needed in addition to the qualitative one. In fact, looking at Fig. 5, we can see that both schemes recognized the desired more external boundary. But analyzing the errors reported in Table 7, we observe that the AF-LW scheme produces lower values in both errors $P-Err_{rel}$ and $P-Err_1$ with respect to the monotone scheme for both the resolutions considered (input image size 170×170 and 340×340). The errors in the second row have been computed using the mask visible in Fig. 2 on the right and are related to Fig. 5. Comparing the CPU time with the two different resolutions, we note that with half time and half size we can obtain better accuracy with respect to the $P-Err_1$ error using the high-order scheme AF-LW instead of the monotone one.

In Tab. 8 we reported the CPU times in seconds related to the brain expansion tests illustrated in Fig. 3 and Fig. 4 for both schemes. We can see that all the tests are fast, needing

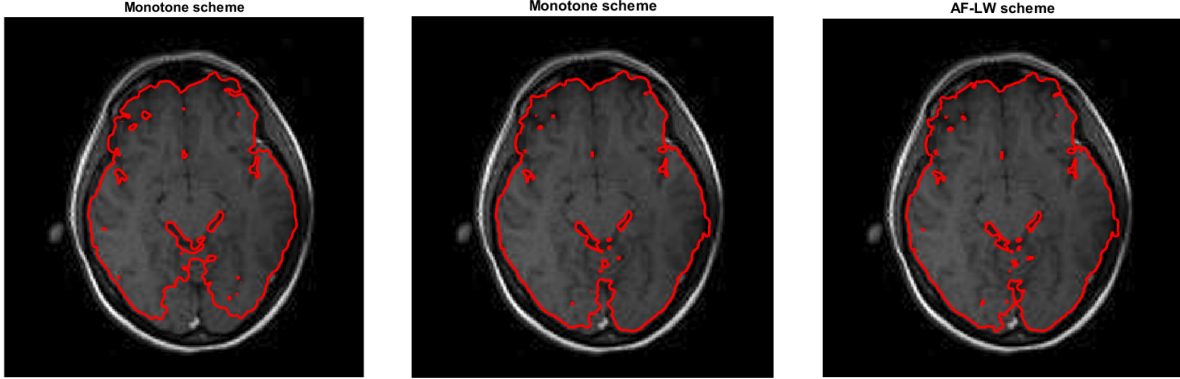


Figure 3: (Test 2a) Datum 1. Plots of the final front using the monotone scheme with $tol = 0.00001$, $N_i = 376$ (left), and with $tol = 0.000005$, $N_i = 468$ (middle), and using the AF-LW scheme with $tol = 0.00001$, $N_i = 407$ (right), all using L^1 norm in the stopping criterion, with $\mu = 4$, $K_{reg} = 5$, and velocity \tilde{c} .

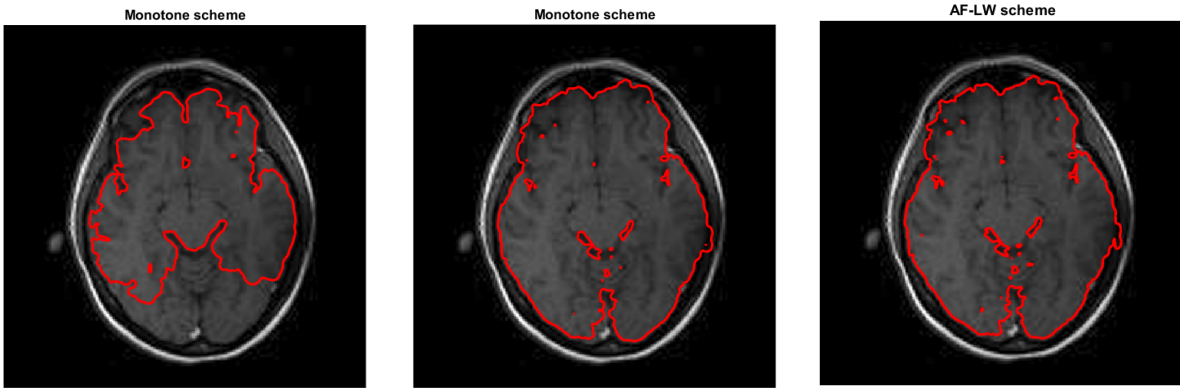


Figure 4: (Test 2a) Datum 2. Plots of the final front using the monotone scheme with $tol = 0.00005$, $N_i = 264$ (left), and with $tol = 0.00001$, $N_i = 495$ (middle), and using the AF-LW scheme with $tol = 0.00005$, $N_i = 431$ (right), all using L^1 norm in the stopping criterion, with $\mu = 4$, $K_{reg} = 5$, and velocity \tilde{c} .

Table 7: (Test 2b) Errors, number of iterations and CPU time in seconds using L^1 norm, \tilde{c} and the parameters $tol = 0.00005$, $\mu = 5$, $K_{reg} = 3$, varying the image size.

Image size	Monotone				AF-LW			
	N_i	(sec.)	$P-Err_{rel}$	$P-Err_1$	N_i	(sec.)	$P-Err_{rel}$	$P-Err_1$
170×170	83	1.14	0.0465	0.2436	87	5.07	0.0439	0.2300
340×340	228	11.67	0.0118	0.2476	262	63.04	0.0078	0.1628

about one minute and half in the worst case. The AF-LW scheme need of course more time, due to the computation of the smoothness indicators, but in any case it is still fast and competitive.

5.2.2 Test 3. Pneumonia

Finally, we conclude our numerical tests by proposing a more complex disposition of the initial condition, which naturally leads to collapsing and merging fronts. We consider a Pneumonia

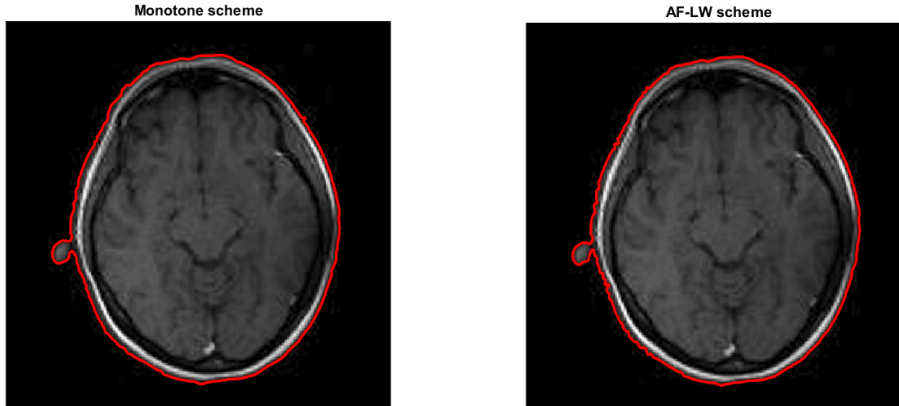


Figure 5: (Test 2b) Plots of the final front using the monotone scheme (left) and the AF-LW scheme (right) with $\mu = 5$, $K_{reg} = 3$, and velocity \tilde{c} . Image size: 340×340 .

Table 8: (Test 2a) CPU times in seconds related to the brain tests (Figs. 3-4).

Figure	Monotone (left)	Monotone (middle)	AF-LW (right)
3	15.96	20.81	77.73
4	11.63	24.58	91.41

image (Input image size: 191×150 pixels) in the expansion case starting from an initial datum here composed by four equal paraboloids (each defined as Datum 1) or cones (defined as Datum 2), placed as visible in Fig. 6, with 0-level sets composed by circles of radius $r = 0.125$.

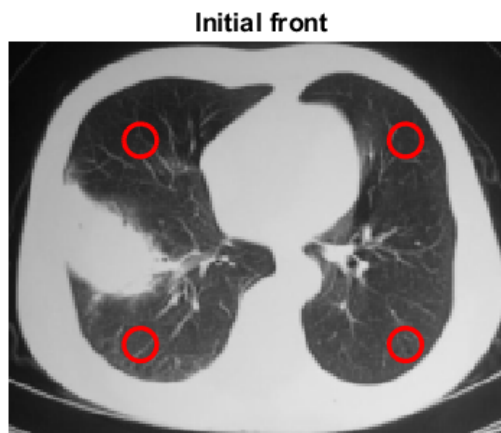


Figure 6: (Test 3a) Initial front composed of four separate circles of radius $r = 0.125$.

We show in Figures 7 and 8 the results obtained by the schemes starting from the two different initial data, Datum 1 and Datum 2, respectively. Looking at the two Figures, it is evident that the AF-LW scheme produces better results using both initial conditions. In fact, in the first figure, Fig. 7, it is evident looking at the lung on the left for both schemes; in the second case, Fig. 8, it is clear especially looking at the right lung. Moreover, comparing in vertical the two figures, focusing on each scheme with different initial datum, we can note that for both schemes the results vary changing the initial condition, with better results when we use the distance

function (Datum 2). The good behavior of the AF scheme and of the modified model in the case of a merging fronts is confirmed by the contour plots of the final representations, shown in Fig. 9.

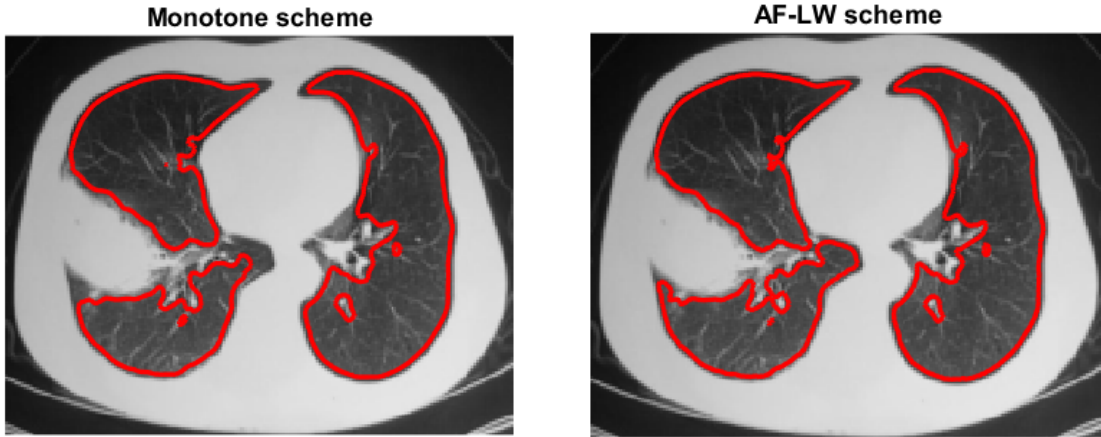


Figure 7: (Test 3a) Datum 1. Plots of the final front using the monotone scheme ($N_i = 185$), and the AF-LW scheme ($N_i = 194$), with L^1 norm and $tol = 0.00001$, $\mu = 4$, $K_{reg} = 5$, and velocity \tilde{c} .

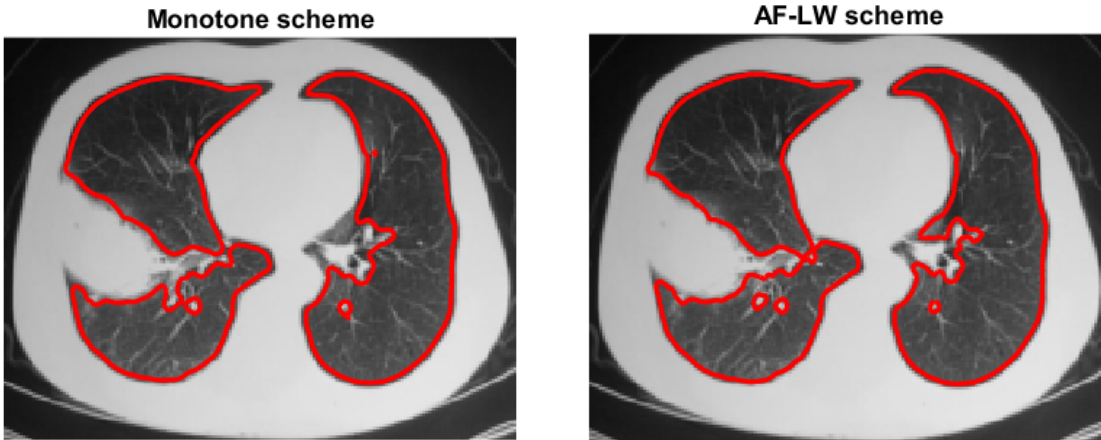


Figure 8: (Test 3a) Datum 2. Plots of the final front using the monotone scheme ($N_i = 413$), and the AF-LW scheme ($N_i = 589$), with L^1 norm and $tol = 0.00001$, $\mu = 4$, $K_{reg} = 5$, and velocity \tilde{c} .

The CPU times in seconds related to the pneumonia tests illustrated starting from Datum 1 (Fig. 7) and Datum 2 (Fig. 8) are reported in Tab. 9. We can note that both schemes run and got convergence in few seconds. The AF-LW scheme runs in a longer time but also in that case time is still contained.

Table 9: (Test 3a) CPU times in seconds related to the Pneumonia tests (Figs. 7-8).

Figure	Monotone	AF-LW
7	2.26	10.66
8	5.60	36.28

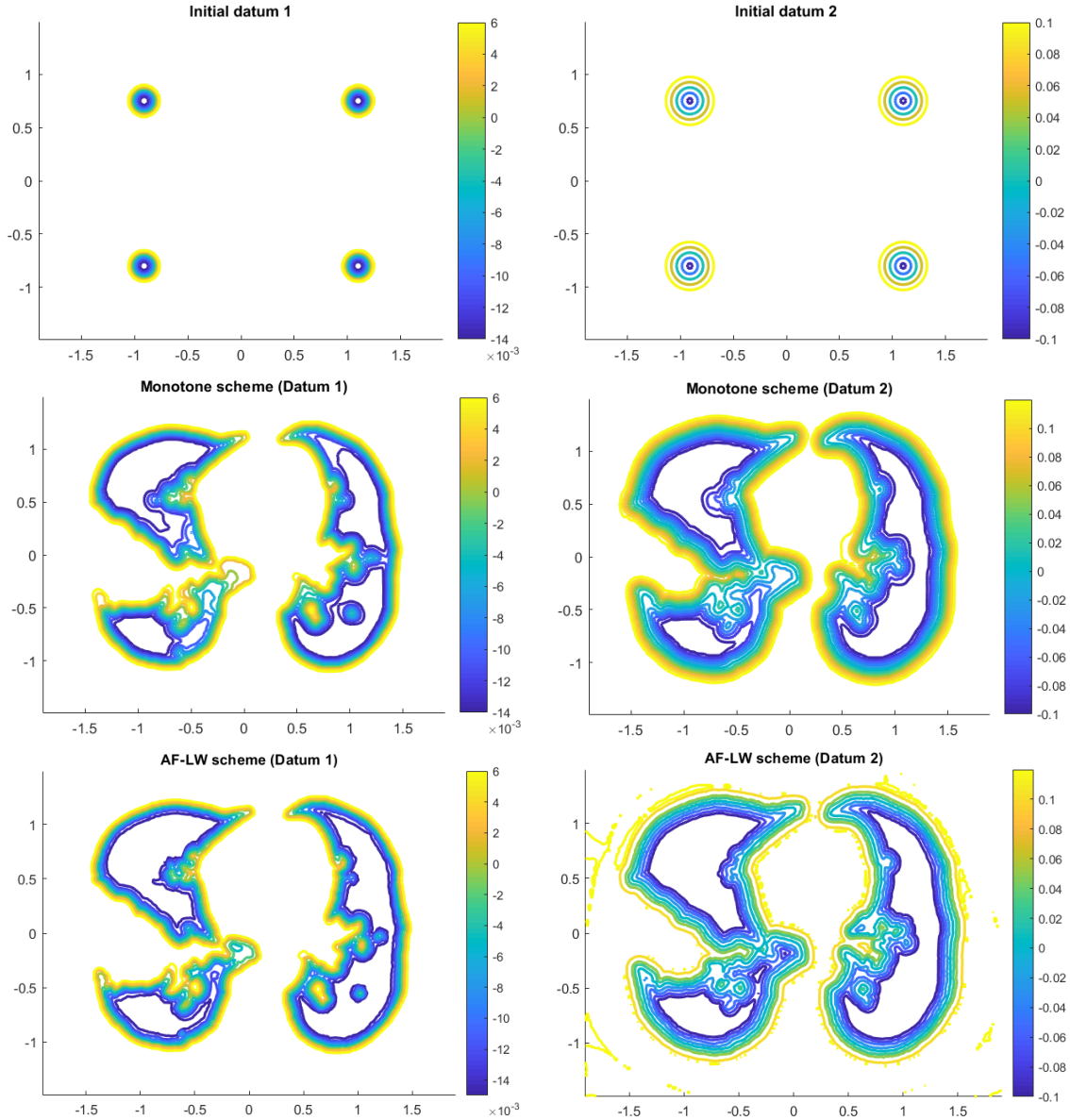


Figure 9: (Test 3a) Contour plots of the initial datum (first row) and the final representations using the monotone scheme (second row) and the AF-LW scheme (last row). Left: Datum 1, right: Datum 2.

6 Conclusions and perspectives

In this work we have proposed a new velocity function in the level-set method used for the image segmentation problem. From the numerical point of view, we have solved the problem in an accurate way by using the AF scheme. We have shown that the use of the new velocity function \tilde{c} is necessary when using high-order scheme as the AF scheme introduced here, but also the simple monotone scheme can benefit of this new velocity function, improving its results with respect to those obtained by using the classical velocity. Moreover, the initial datum seems to play a role for the AF scheme, with a small preference for the Datum 2, whereas the monotone scheme seems not to be a lot influenced by it. The numerical tests confirm the effectiveness of

the proposed method, getting better performances with respect to the monotone scheme. In the future, we want to investigate more the use of different filter functions F or different smoothness indicator functions $\phi_{i,j}^n$, in order to improve more the results, if possible. Further extensions to second order problems could also be considered in a future work.

References

- [1] S. Amat, F. Aràndiga, A. Cohen, and R. Donat. Tensor product multiresolution analysis with error control for compact image representation. *Signal Processing*, 82(4):587–608, 2002.
- [2] F. Aràndiga, A. M. Belda, and P. Mulet. Point-value weno multiresolution applications to stable image compression. *Journal of Scientific Computing*, 43(2):158–182, May 2010.
- [3] F. Aràndiga and A.M. Belda. Weighted ENO interpolation and applications. *Commun. Nonlinear Sci. Numer. Simul.*, 9(2):187–195, 2003.
- [4] G. Barles. *Solutions de viscosité des équations de Hamilton-Jacobi*. Springer Verlag, 1994.
- [5] O. Bokanowski, M. Falcone, and S. Sahu. An efficient filtered scheme for some first order Hamilton-Jacobi-Bellman equations. *SIAM J. Sci. Comput.*, 38(1):A171–A195, 2016.
- [6] T. Brox and J. Weickert. Level Set Based Image Segmentation with Multiple Regions. In Carl Edward Rasmussen, Heinrich H. Bülthoff, Bernhard Schölkopf, and Martin A. Giese, editors, *Pattern Recognition*, pages 415–423, Berlin, Heidelberg, 2004. Springer Berlin Heidelberg.
- [7] X. Cai, R. Chan, and T. Zeng. A Two-Stage Image Segmentation Method Using a Convex Variant of the Mumford–Shah Model and Thresholding. *SIAM Journal on Imaging Sciences*, 6(1):368–390, 2013.
- [8] V. Caselles, F. Catté, T. Coll, and F. Dibos. A geometric model for active contours in image processing. *Num. Math.*, 66:1–31, 1993.
- [9] V. Caselles, R. Kimmel, and G. Sapiro. Geodesic Active Contours. *International Journal of Computer Vision*, 22(1):61–79, Feb 1997.
- [10] M.G. Crandall and P.-L. Lions. Viscosity solutions of Hamilton-Jacobi equations. *Transactions of the American Mathematical Society*, 277(1):1–42, 1983.
- [11] M. Falcone, G. Paolucci, and S. Tozza. Convergence of Adaptive Filtered schemes for first order evolutive Hamilton-Jacobi equations. 2018, submitted. arXiv:1812.02140.
- [12] M. Falcone, G. Paolucci, and S. Tozza. Adaptive Filtered Schemes for first order Hamilton-Jacobi equations. In F.A. Radu, K. Kumar, I. Berre, J.M. Nordbotten, and I.S. Pop, editors, *Numerical Mathematics and Advanced Applications ENUMATH 2017*. Springer, to appear.
- [13] A. Harten, S. Osher, B. Engquist, and S. R. Chakravarthy. Some results on uniformly high-order accurate essentially nonoscillatory schemes. *Appl. Numer. Math.*, 2(3-5):347–377, 1986.
- [14] A. K. Henrick, T. D. Aslam, and J. M. Powers. Mapped weighted essentially non-oscillatory schemes: Achieving optimal order near critical points. *J. Comput. Phys.*, 207:542–567, 2005.
- [15] G.-S. Jiang and C.-W. Shu. Efficient implementation of weighted ENO schemes. *J. Comput. Phys.*, 126(1):202–228, 1996.
- [16] P.L. Lions and P. Souganidis. Convergence of MUSCL and filtered schemes for scalar conservation laws and Hamilton–Jacobi equations. *Num. Math.*, 69:441–470, 1995.
- [17] X.D. Liu, S. Osher, and T. Chan. Weighted essentially non-oscillatory schemes. *J. Comput. Phys.*, 115(1):200–212, 1994.

- [18] R. Malladi, J. A. Sethian, and B. C. Vemuri. Shape modeling with front propagation: a level set approach. *IEEE Transactions on Pattern Analysis and Machine Intelligence*, 17(2):158–175, Feb 1995.
- [19] A. M. Oberman and T. Salvador. Filtered schemes for Hamilton-Jacobi equations: a simple construction of convergent accurate difference schemes. *Journal of Computational Physics*, 284:367–388, 2015.
- [20] S. Osher and R. Fedkiw. *Level Set Methods and Dynamic Implicit Surfaces*. Springer, 2003.
- [21] S. Osher and J. A. Sethian. Fronts propagating with curvature-dependent speed: Algorithms based on Hamilton-Jacobi formulations. *Journal of Computational Physics*, 79(1):12–49, November 1988.
- [22] S. Osher and C.-W. Shu. High-order essentially non oscillatory schemes for Hamilton-Jacobi equations. *SIAM J. Numer. Anal.*, 28(4):907–922, 1991.
- [23] G. Paolucci. *Adaptive Filtered Schemes for first order Hamilton-Jacobi equations and applications*. PhD thesis, Dipartimento di Matematica, Sapienza - Università di Roma, Italy, July 2018.
- [24] J. A. Sethian. Curvature and the evolution of fronts. *Commun. in Mathematical Physics*, 101:487–499, 1985.
- [25] J.A. Sethian. *Level Set Methods and Fast Marching Methods: Evolving Interfaces in Computational Geometry, Fluid Mechanics, Computer Vision, and Materials Science*. Cambridge University Press, 2nd edition, 1999.
- [26] K. Zhang, L. Zhang, K.-M. Lam, and D. Zhang. A level set approach to image segmentation with intensity inhomogeneity. *IEEE Transactions on Cybernetics*, 46(2):546–557, 2016.
- [27] Y.T. Zhang and C.-W. Shu. ENO and WENO schemes. In *Handbook of numerical methods for hyperbolic problems*, pages 103–122. Elsevier/North-Holland, 2016.